

Dissolution of randomly distributed soluble grains: post-dissolution k_0 -loading and shear

M. CHA* and J. C. SANTAMARINA*

Sediments experience mineral dissolution in most natural settings, and as a result of engineered processes such as carbon dioxide injection. The consequences of mineral dissolution are studied using the three-dimensional discrete-element method by gradually dissolving randomly distributed soluble grains in a laterally constrained cell under constant vertical stress. Either additional vertical load under zero lateral strain or shear loading are applied after dissolution. Results show that dissolution is accompanied by global horizontal stress change, increase in vertical displacement and porosity, and decrease in coordination number. Post-dissolution, sediments are more compressible; shear loading encounters a diminished peak strength and reduced dilative tendency in sediments that experienced dissolution; however, all specimens evolve towards a common ‘critical state’ strength and sediment fabric at a large strain (in the absence of reprecipitation, changes in grain shape, or changes in grain size distribution). The analysis of micromechanical parameters shows that the total number of contacts decreases during dissolution and remaining contacts carry higher forces. Higher granular interlocking hinders settlement and leads to the development of higher fabric and force anisotropy during dissolution. Granular arching effectively resists vertical displacement around dissolving grains, a honeycomb fabric emerges and the specimen gains a higher porosity during dissolution. Overall, the extent of dissolution (soluble fraction) and the level of particle interlocking/angularity define the evolution of micro- and macro-scale parameters during dissolution and its response to subsequent loading.

KEYWORDS: collapsed settlement; compressibility; discrete-element modelling; earth pressure; fabric/structure of soils; particle-scale behaviour; shear strength

INTRODUCTION

Mineral dissolution is a common chemical weathering and diagenetic process in geological systems. Typically, the time scale is long and mineral dissolution is disregarded in most engineering designs. However, this may not be the case when minerals such as carbonates and/or acidic fluids are involved, and when projects have a long design life, such as carbon dioxide storage.

Dissolution is responsible for karst structures (Ford & Williams, 2007; Waltham, 2009), may cause the formation of polygonal faults observed in marine basins (Cartwright & Dewhurst, 1998; Shin *et al.*, 2008) and can accelerate piping erosion, increase uplift pressure and compromise the stability of dams (Unay *et al.*, 1982; Dreybrodt *et al.*, 2002; Pearson, 2002; Gutiérrez *et al.*, 2003; Jarvis, 2003; Payton & Hansen, 2003; Craft *et al.*, 2006; Johnson, 2008). Dissolution and reprecipitation change volcanic ash from a sediment with a void ratio $e = 0.8 \sim 1.5$ and specific surface $S_s = 0.1 \sim 1 \text{ m}^2/\text{g}$ to a sediment with $e = 2 \sim 7$ and $S_s = 50 \sim 200 \text{ m}^2/\text{g}$ (Herrera *et al.*, 2007). Fluid permeability changes (Zheng & Elsworth, 2012) and chemically induced compaction bands have been attributed to dissolution coupled with grain breakage (Stefanou & Sulem, 2014).

Human activity may accelerate dissolution. The geological storage of carbon dioxide is of particular interest in this context: carbon dioxide dissolution acidifies water and prompts mineral dissolution (Cowan & Weintritt, 1976;

Montes-Hernandez *et al.*, 2007; Espinoza *et al.*, 2011). The ensuing hydro-chemo-mechanical coupling can lead to porosity and mineralogy changes, settlement, tensile fracturing of the seal caprock, piping and shear failure in compression (He *et al.*, 2003; Watson *et al.*, 2004; Renard *et al.*, 2005; Le Guen *et al.*, 2007; Espinoza *et al.*, 2011). Therefore, the analysis of carbon dioxide geological storage must consider the possible consequences of mineral dissolution.

Non-mineral solid phases may also vanish, such as ice in frozen ground or methane hydrate in marine sediments or in permafrost settings (Rothwell *et al.*, 1998; Vogt & Jung, 2002; Sultan *et al.*, 2004; Freij-Ayoub *et al.*, 2007; Lee *et al.*, 2010).

Particle-scale dissolution affects small- and large-strain properties. The sediment contracts yet the void ratio increases during dissolution (Fam *et al.*, 2002; Shin & Santamarina, 2009; Truong *et al.*, 2010; Muir Wood *et al.*, 2010; Tran *et al.*, 2012; McDougall *et al.*, 2013a, 2013b) and a ‘honeycomb fabric’ emerges (Shin *et al.*, 2008; Shin & Santamarina, 2009). The value of k_0 decreases often to k_a before it recovers (experiments in Shin & Santamarina (2009)), and shear wave velocity decreases and attenuation increases during dissolution (Fam *et al.*, 2002; Truong *et al.*, 2010; Lee *et al.*, 2012). The peak friction angle is lower after dissolution (Fam *et al.*, 2002, Tran *et al.*, 2012) and the cone penetration resistance decreases with increasing dissolution (Cha & Santamarina, 2013).

In this study, an investigation is carried out into the behaviour of coarse-grained sediments during dissolution, post-dissolution k_0 -loading and post-dissolution simple shear loading using the discrete-element method (DEM) in three dimensions. There are various possible modes of mineral dissolution in sediments, such as dissolution of homogeneously distributed soluble mineral grains, localised dissolution as a result of

Manuscript received 23 June 2014; revised manuscript accepted 12 August 2014. Published online ahead of print 3 October 2014.

Discussion on this paper closes on 1 March 2015, for further details see p. ii.

*School of Civil and Environmental Engineering, Georgia Institute of Technology, Atlanta, GA, USA.

hydro-chemo-mechanical coupling, dissolution of concentrated dissolvable anomalies and pressure solution. This study addresses the first case – that is, the dissolution of homogeneously distributed dissolvable grains.

SIMULATION APPROACH

Dissolution is performed in a numerical three-dimensional (3D) cell with zero lateral strain side-walls (PFC-3D (Cundall & Strack, 1979)). Spherical particles with uniform grain size distribution ($R_{min} = 1 \text{ mm}$, $R_{max} = 1.5 \text{ mm}$ – see Table 1) are packed by randomly placing smaller grains in the cube and gradually expanding them under zero gravity and zero interparticle friction to attain the target porosity ($n \approx 0.38$). Then, friction and gravity are turned on, and the specimen is incrementally loaded in the vertical direction to $\sigma_v = 100 \text{ kPa}$ under zero lateral strain conditions.

Different soluble fractions (SF) are simulated, where SF is defined as the mass of soluble particles with respect to the total mass. Soluble particles are randomly assigned in the preformed granular packing (see Fig. 1). Dissolution under

constant servo-controlled vertical stress and zero lateral strain $\epsilon_h = 0$ is simulated by gradually reducing the radius of all the soluble particles at the same rate (Fig. 1). The ratio of the mean unbalanced force to the mean contact force is always smaller than 0.001 to ensure stable conditions throughout the dissolution processes. After dissolution, the specimen is either loaded at zero lateral strain to assess k_0 compressibility, or subjected to simple shear to evaluate shear resistance and volume change (Fig. 1). Basic model properties and the simulation environment are summarised in Table 1.

Particle rotation and angularity: spherical particles rotate more freely than non-spherical particles found in real sediments where interlocking inhibits rotation. Although particle rotation has a limited effect on elastic properties, it alters shear resistance and volume change (Bardet & Proubet, 1991; Bardet, 1994; Iwashita & Oda, 1998; Mohamed & Gutierrez, 2010). In this study, rotation is hindered on preselected particles as a numerical proxy for angularity and interlocking (Rothenburg & Bathurst, 1993; Bardet, 1994; Iwashita & Oda, 1998, 2000; Thomas & Bray, 1999; Mirghasemi *et al.*, 2002; Suiker & Fleck, 2004).

Table 1. Model properties and simulation environment (code: PFC-3D)

	Properties	Values
Ball	Initial radius of balls	Uniform size distribution ($R_{min} = 1 \text{ mm}$, $R_{max} = 1.5 \text{ mm}$)
	Number of balls	9167
	Mass density of balls	2650 kg/m ³
	Hertzian contact model	Shear modulus = $2.9 \times 10^9 \text{ Pa}$ Poisson ratio = 0.3
Boundary conditions	Inter-particle friction	0.5
	Initial cell size	(Height \times width \times length) 5 cm \times 5 cm \times 5 cm
	Vertical load	100 kPa (during dissolution)
	Zero lateral strain	
	Particle-to-wall friction	0

Summary of parametric study: fraction of soluble particles SF = 0, 2, 5, 10, 15 and 25%; fraction of particles with hindered rotation HR = 0, 40 and 80%; main control variable: size reduction of soluble particles $\Delta R/R_0$.

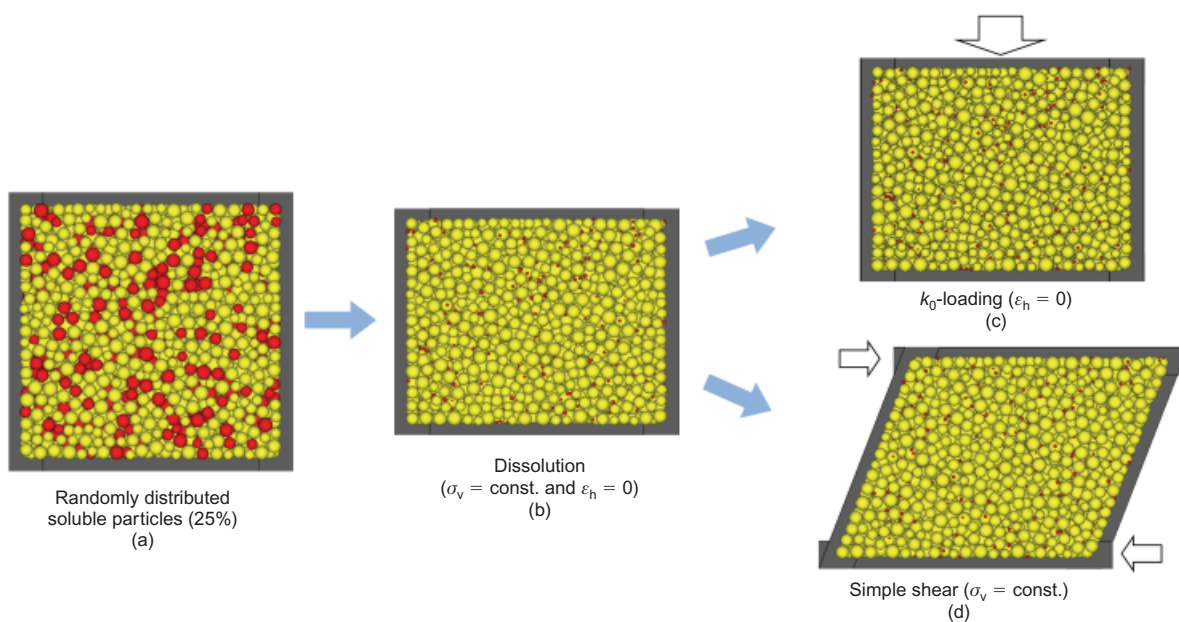


Fig. 1. Simulation sequence in DEM 3D: (a) initial packing; (b) after dissolution; (c) post-dissolution vertical loading under zero lateral strain; (d) post-dissolution shear loading. Images shown for a soluble fraction SF = 25%

RESULTS: MACRO-SCALE OBSERVATIONS

The parametric study considers various fractions of soluble particles (SF% = 0, 2, 5, 10, 15, 25), different fractions of particles with hindered rotation (HR% = 0, 40, 80) and three simulation stages: dissolution, post-dissolution k_0 -loading and post-dissolution simple shear loading. Macro-scale results for each stage are presented first.

Sediment evolution during dissolution ($\sigma_v = \text{constant}$; $\epsilon_h = 0$)

The evolution of vertical displacement, porosity and equivalent global stress ratio k_0 during dissolution at constant vertical stress $\sigma'_v = 100$ kPa and zero lateral strain $\epsilon_h = 0$ are plotted in Fig. 2 as a function of the size reduction $\Delta R/R_0$ experienced by the randomly selected dissolving particles. Results are shown for sediments with different fractions of soluble particles SF, without hindered rotation, HR = 0%.

Normalised vertical displacement: sediments contract and settle during dissolution (Fig. 2(a)). For settlements during early stages of dissolution (i.e. low $\Delta R/R_0$) or for sediments with low percentage of soluble particles SFs are small as particle-level forces arch to redistribute the force relinquished by dissolving particles (Shin *et al.*, 2008). However, the sediment response is different for the same mass loss if (a) the soluble fraction SF is low or (b) during early stages of dissolution in sediments with high soluble fraction SF > 10%

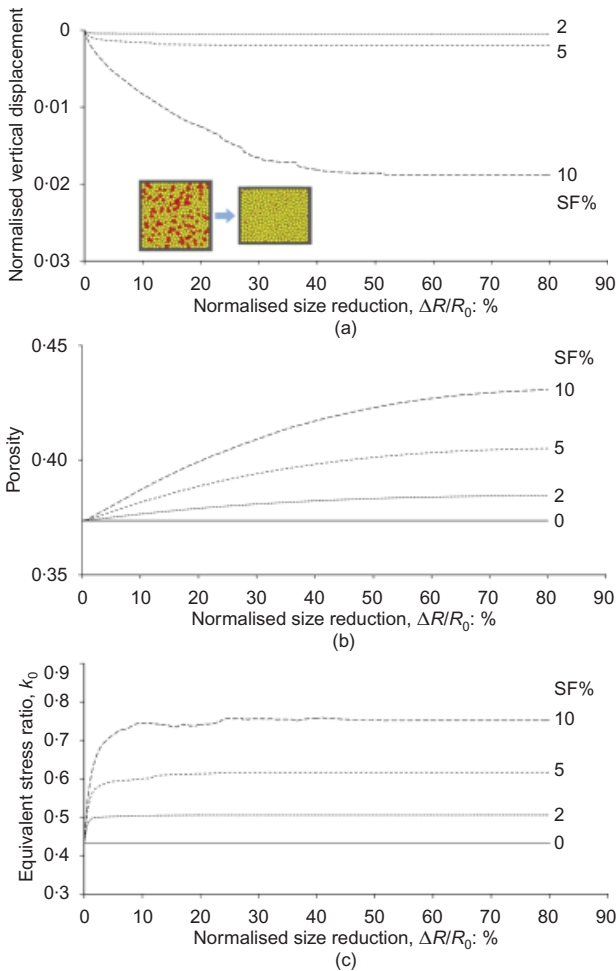


Fig. 2. Sediment response during dissolution under $\sigma_v = 100$ kPa and $\epsilon_h = 0$ (no hindered rotation, HR = 0%): (a) normalised vertical displacement; (b) porosity; (c) equivalent global stress ratio k_0 under a zero lateral strain condition. Trends shown for different soluble fractions SF

(applies to all parameters including displacement and porosity): soluble grains distributed throughout the soil mass in high-SF specimens are more disruptive to force chains.

Porosity: porosity increases proportionally to the soluble fractions SF as dissolution progresses $\Delta R/R_0$ (Fig. 2(b)). The increase in porosity tends to an asymptotic value for each sediment.

Equivalent global stress ratio k_0 : all specimens show an increase in equivalent global stress ratio k_0 during dissolution when interlocking is not enforced by hindered rotation (HR = 0%). The asymptotic k_0 value increases with increasing fraction of soluble particles SF (Fig. 2(c)).

Angularity and interlocking – hindered rotation: some experimental results obtained for sand–salt mixtures show that k_0 may decrease to k_a during dissolution (contrary to trends in Fig. 2), and it may eventually recover if dissolution continues (Shin *et al.*, 2008; Shin & Santamarina, 2009). Numerical results plotted in Fig. 3 show that experimental trends are matched when the percentage of particles with hindered rotation is relatively high, HR → 80%. All numerical simulations conducted as part of this study were repeated with various levels of hindered rotation. Trends are bracketed by results obtained with HR = 0% (i.e. smooth spherical particles – no numerical proxies) and HR = 80% (i.e. interlocking angular particles).

Post-dissolution k_0 vertical loading ($\epsilon_h = 0$)

The post-dissolution sediment response to vertical loading under zero lateral strain $\epsilon_h = 0$ is investigated to assess changes in compressibility. Results show that the vertical displacement is higher for specimens that experienced more extensive dissolution (Fig. 4(a)). Porosity decreases with increasing vertical stress, although the magnitude of volume contraction for an order of magnitude increase in stress is relatively small compared to the gain in porosity during dissolution (Fig. 4(b)). The internal sediment structure is relatively unaffected by post-dissolution k_0 -loading (for an order of magnitude increase in stress). In the absence of interlocking (SF = 0%), the equivalent global stress ratio k_0 decreases upon loading (Fig. 4(c)).

Post-dissolution simple shear loading

The same post-dissolution sediments tested above are subjected to simple shear under constant vertical stress $\sigma_v = \text{const}$. Numerical results show a pronounced decrease in

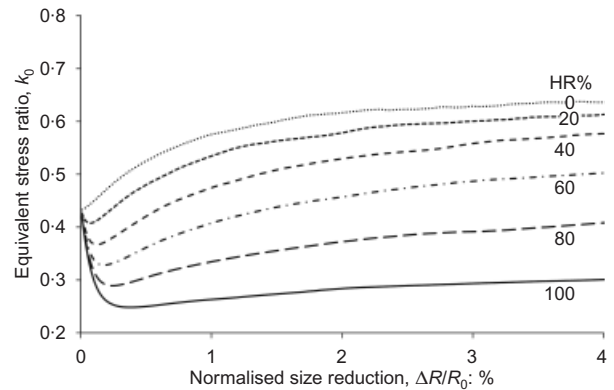


Fig. 3. The effect of hindered rotation HR during dissolution ($\sigma_v = 100$ kPa; $\epsilon_h = 0$; soluble particles SF = 25%). The evolution of the equivalent stress ratio k_0 as a function of dissolution in terms of size reduction $\Delta R/R_0$ and hindered rotation HR. Results shown for early stages of dissolution $\Delta R/R_0 \leq 4\%$ to highlight the reduction in k_0

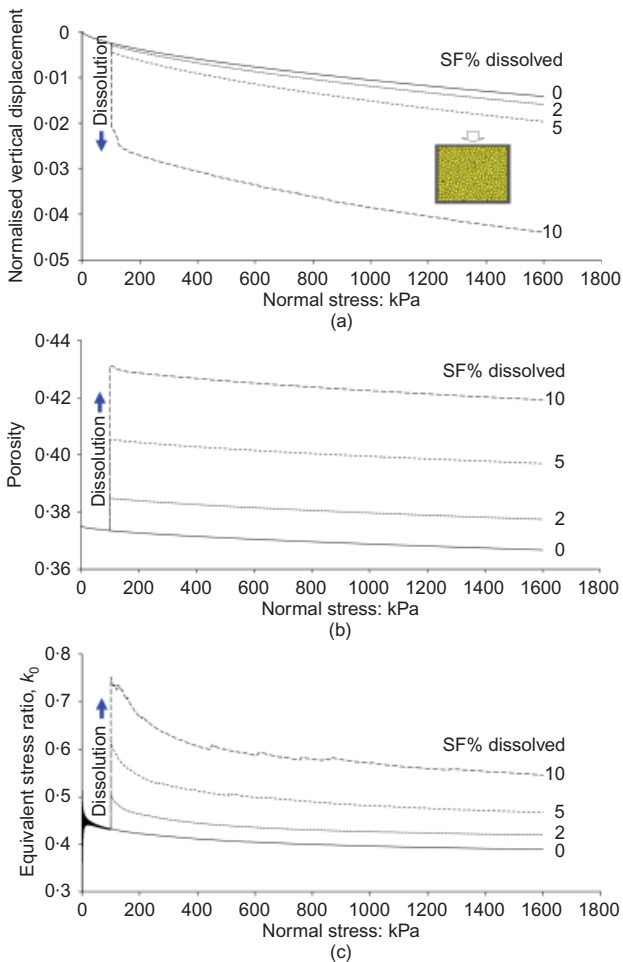


Fig. 4. Post-dissolution response to additional k_0 -loading ($\epsilon_h = 0$; no hindered rotation, $HR = 0\%$): (a) normalised vertical displacement; (b) porosity; (c) equivalent global stress ratio k_0 under a zero lateral strain condition. Trends shown for different soluble fractions SF

shear stiffness with the increase in soluble fraction SF (Fig. 5(a)). The dilative tendency decreases as the soluble fraction SF increases (Fig. 5(b)); eventually the sediment becomes contractive (when $SF \geq 10\%$ in this case). Void ratio and shear resistance tend to a common ‘critical state’ for all specimens at large strains (Figs 5(a) and 5(c)). The increase in contractive tendency with increased post-dissolution void ratio (i.e. state parameter) is in agreement with standard soil behaviour response (Been & Jefferies, 1985; Muir Wood *et al.*, 2010).

RESULTS: PARTICLE-LEVEL OBSERVATIONS

Coordination number: the average number of contacts per particle is a measure of fabric stability. The code PFC identifies ‘real’ and ‘virtual’ contacts: ‘real’ contacts have larger forces and particle overlap, whereas ‘virtual’ contacts correspond to particle separations less than 10^{-6} times the mean radius. (Note: the coordination number based on ‘real’ contacts may not satisfy the minimum coordination for equilibrium.)

Coordination numbers based on real and virtual contacts are plotted for all states and specimens in Fig. 6. The coordination number decreases as dissolution $\Delta R/R_0$ progresses and the initial soluble fraction SF increases; this observation applies whether all contacts or only real contacts are considered (Fig. 6(a)). Coordination numbers increase slightly with normal stress under k_0 -loading, and they evolve

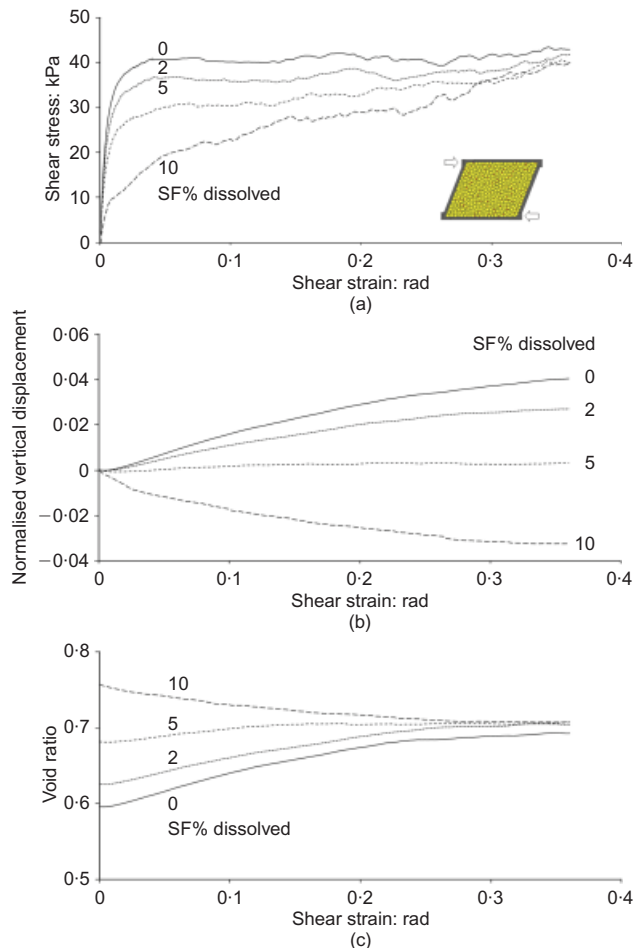


Fig. 5. Post-dissolution response to simple shear loading ($\sigma'_v = 100$ kPa; hindered rotation $HR = 0\%$): (a) shear stress; (b) normalised vertical displacement; (c) void ratio. Trends shown for different soluble fractions SF

towards a common value at large shear strains for all sediments – that is, a ‘critical state’ fabric (Fig. 6(c)).

Contact forces: histograms of contact forces before and after dissolution are compared in Fig. 7 for quasi-horizontal contact forces (taking into consideration all contact forces at $\pm 30^\circ$ from horizontal) and quasi-vertical contact forces (all contact forces at $\pm 30^\circ$ from vertical). The total number of contacts decreases, higher contact forces are mobilised both in the vertical and horizontal directions, and the number of contacts with lower contact forces decreases after dissolution.

Polar plots: polar plots of micromechanical parameters are shown in Fig. 8 for specimens made of rounded particles without hindered rotation ($HR = 0\%$; $SF = 2\%$ and 10%) and in Fig. 9 for an interlocked specimen ($HR = 80\%$; $SF = 10\%$). Anisotropy parameters used to fit the first-order Fourier series to the polar plots are noted in each case (as in Rothenburg & Bathurst, 1989). Internal anisotropy decreases during dissolution when rounded particles are involved (Fig. 8 – $HR = 0\%$). By contrast, internal anisotropy increases during dissolution in granular packings that experience interlocking, and the peak internal anisotropy is reached when the global stress ratio is minimum (Fig. 9 – $HR = 80\%$). It can be concluded that interlocking by hindered rotation hampers structural rearrangement and the sediment must mobilise higher internal anisotropy to undertake the applied load.

DISCUSSION: VOID AND SOLID PHASE VOLUMES

Gravimetric–volumetric relations allow the tracking of volume of voids V_V and the volume of the solid phase V_S

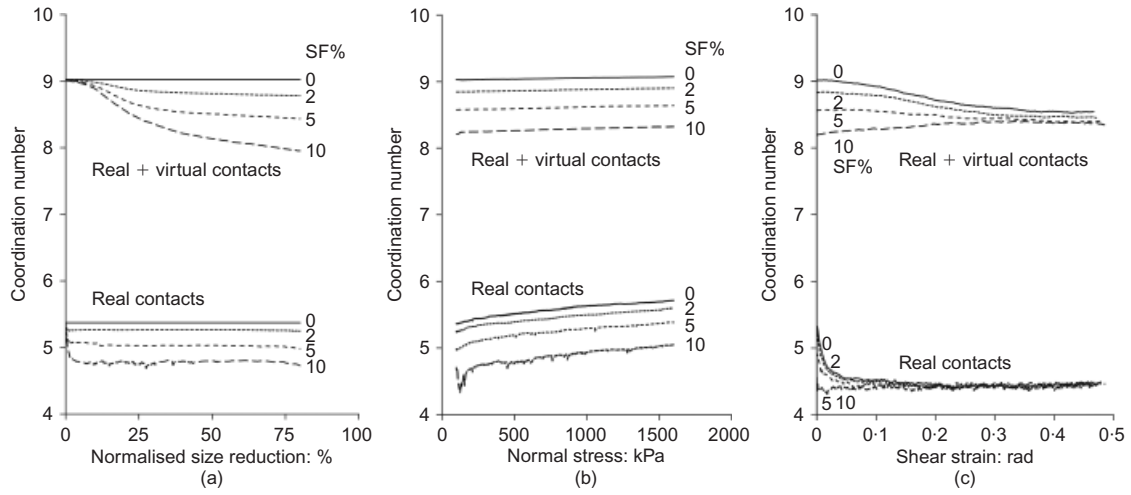


Fig. 6. Coordination number during: (a) dissolution ($\sigma_v = 100$ kPa, $\varepsilon_h = 0$); (b) post-dissolution k_0 -loading; (c) post-dissolution simple shear. Note: no hindered rotation (HR = 0%)

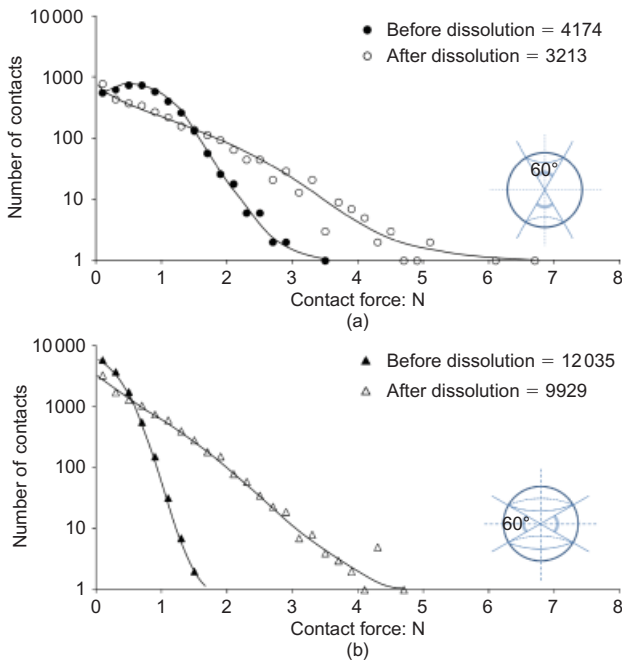


Fig. 7. Histogram of contact forces before and after dissolution for (a) quasi-vertical ($\pm 30^\circ$ from vertical) and (b) quasi-horizontal contacts ($\pm 30^\circ$ from horizontal) – soluble fraction SF = 10%, no hindered rotation, HR = 0%

from experimental or numerically measured quantities, such as

$$V_{Si} = V_{S0} \left(1 - \frac{\Delta M_i}{M_0} \right) \quad (1)$$

$$V_{Vi} = V_T - V_{Si} \quad (2)$$

where V_T is the total volume and the subscript i denotes instantaneous values during dissolution. The dissolution-induced void change parameter defined as $\Lambda_i = \partial V_{Vi} / \partial V_{Si}$ shows the rate of change in void volume associated with the change in solid phase volume (McDougall & Pyrah, 2004). The following guidelines facilitate the interpretation of data plotted in terms of volume of void V_V against volume of the solid phase V_S (refer to Fig. 10(a)).

- The instantaneous void ratio $e_i = V_{Vi} / V_{Si}$ is the slope of the secant to the origin.

- The instantaneous value of the dissolution parameter is the local tangent $\Lambda_i = \partial V_{Vi} / \partial V_{Si}$.
- Instantaneous changes that plot above the e_i line imply increasing void ratio, and below the e_i line correspond to decreasing void ratio.
- Volume changes preserve void ratio when $\Lambda_i = e_i$, occur at constant volume of voids when $\Lambda = 0$, evolve at constant volume of solids when $|\Lambda| = \infty$, and take place at constant total volume when $\Lambda = -1$.

Note that volume changes at constant total volume lead to a realisable upper bound for the change in porosity Δn during dissolution

$$\Delta n = (1 - n_0) \text{SF} \quad (3)$$

Figure 10(b) shows the evolution of the volume of voids V_V plotted against the volume of the solid phase V_S for simulations conducted without hindered rotation HR = 0% and for interlocked packings with hindered rotation HR = 80% and various soluble fractions SF. In general, sediments with a small fraction of soluble particles, SF < 10%, experience mineral dissolution at constant volume $\Lambda = -1$, and the increase in porosity Δn reflects equation (3). Dissolution at constant volume is more pronounced in packings with higher hindered rotation. On the other hand, the total volume readily changes as dissolution takes place in sediments with a high fraction of soluble particles and the dissolution parameter increases and may exceed $\Lambda = 0$.

Instantaneous values of Λ_i during dissolution show significant oscillations that reflect the instantaneous variation in volume of voids and volume of solids resulting from interparticle slippage and granular chain buckling. Arch formation depends on factors such as interparticle friction and particle angularity/interlocking. These force chains form because the force initially carried by a dissolvable grain is transferred to neighbouring grains soon after dissolution starts. When the fraction of soluble particles is small, isolated dissolving grains leave voids behind and neighbouring insoluble particles form an arch around them and hide the void (hence, the total volume change is small, as observed above). Yet, chains formed by insoluble particles buckle more readily when the soluble fraction is high, and the total volume contraction starts tracking the solid volume loss more closely. The causal link between strong force chains and post-dissolution voids is best visualised in two-dimensional (2D) DEM simulations (see honeycomb fabric in Shin & Santamarina (2009)). The 2D cross-correlation

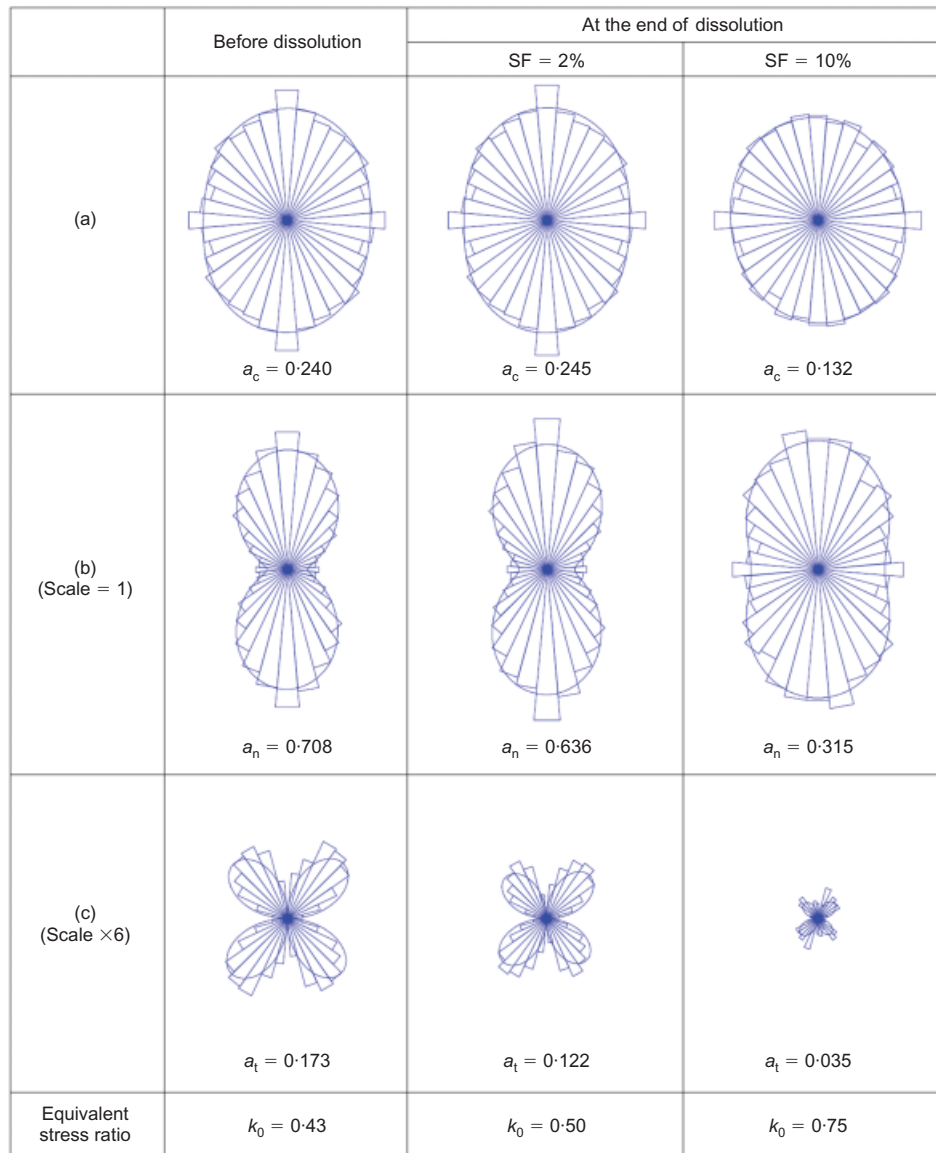


Fig. 8. Polar plots of internal micromechanical parameters before and after dissolution – no hindered rotation, HR=0%: (a) contact density histogram; (b) mean normal contact force; (c) mean tangential contact force

between an image of force chains and an image of voids confirms the intimate correlation between voids and strong forces – see Cha (2012)).

Experimental data obtained with rounded sand and granular salt mixtures show that the average dissolution parameter – from beginning to the end of dissolution – increases with the percentage of soluble salt grains (McDougall *et al.* (2013a) – note: values depend on the relative size of soluble and insoluble grains): from $\Lambda \leq -0.7$ for SF $\leq 5\%$ and reaches $\Lambda \approx -0.35$ for SF = 15%. These trends compare well with simulations for rounded particles HR = 0% presented above: the average dissolution parameter is $\Lambda \approx -1$ when SF $\leq 5\%$, $\Lambda \approx -0.85$ when SF = 10%, $\Lambda \approx -0.35$ when SF = 15%, and $\Lambda \approx +0.15$ when SF = 25%. (For completeness, the average dissolution parameters for angular/interlocked packings are $\Lambda \approx -1$ when SF = 15% and $\Lambda \approx -0.7$ when SF = 25%.)

CONCLUSIONS

Mineral dissolution is a common diagenetic process. In many cases, solid phase loss can take place within the

design life of engineered systems. The loss of solid mass has important particle-scale and macro-scale implications. Numerical results obtained in this study show the following points.

- Grain dissolution at zero lateral strain affects the equivalent global stress ratio k_0 . Its evolution depends on the degree of particle angularity or interlocking. k_0 increases in rounded particles but it decreases – often to k_a – in sediments made of angular/interlocked particles.
- Forces initially carried by dissolvable grains are transferred to neighbouring grains during dissolution. The coordination number decreases and preponderant interparticle force chains form arches around developing voids in a honeycomb-like fabric.
- Force arching is more prevalent in angular/interlocked particles and when the fraction of soluble particles is low, that is SF $< \sim 10\%$. These conditions lessen global volume contraction as the internal porosity increases. Conversely, the total volume responds more readily to mineral dissolution when the percentage of soluble

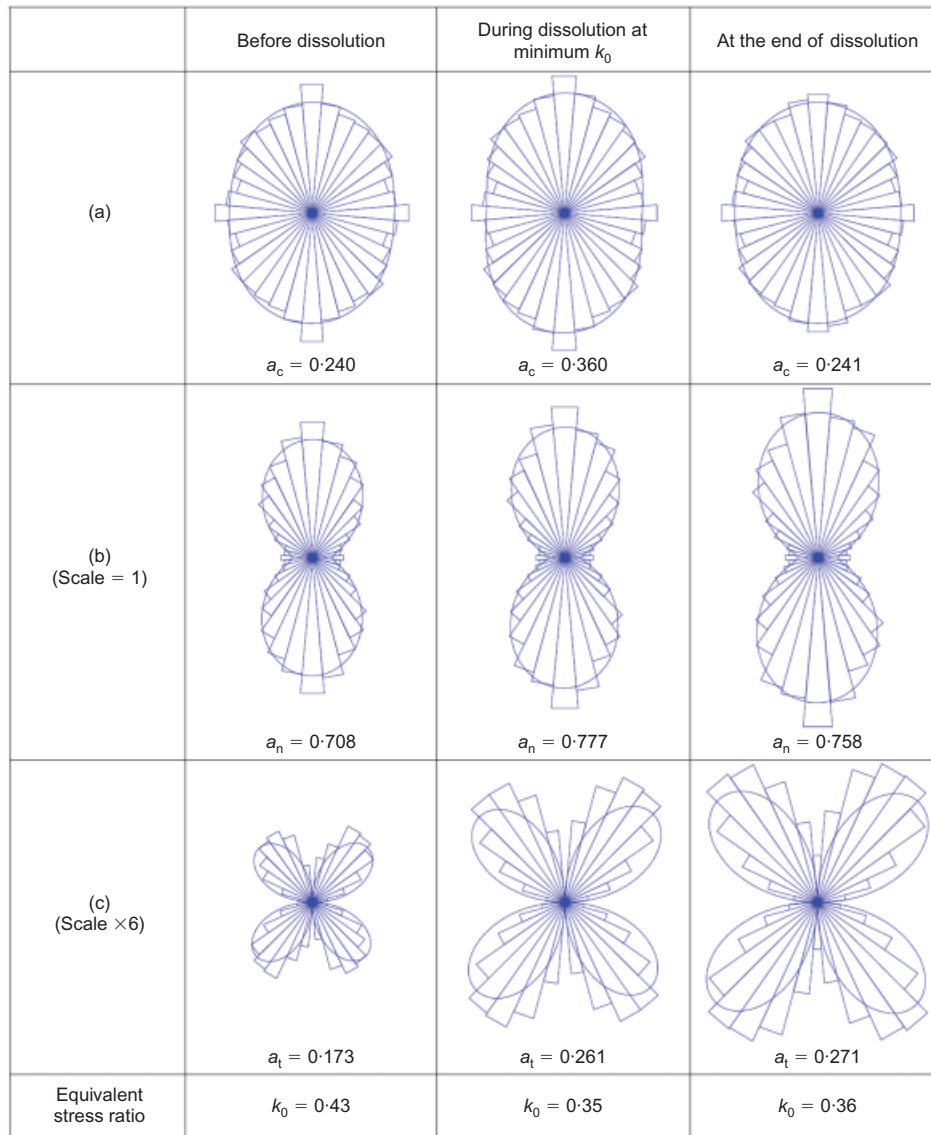


Fig. 9. Polar histograms of internal micromechanical parameters before dissolution, at minimum k_0 , and after dissolution for ‘angular’ particles with hindered rotation $HR = 80\%$ and with a soluble fraction $SF = 10\%$: (a) contact density histogram; (b) mean normal contact force; (c) mean tangential contact force

particles exceeds $SF > \sim 10\%$ as the removal of soluble grains distributed throughout the soil mass in high-SF specimens extensively disrupts force carrying granular chains.

- When dissolution takes place under zero lateral strain conditions, the post-dissolution internal anisotropy is more pronounced in angular/interlocked grains than in specimens made of round particles.
- Sediments are more compressible after dissolution. The increase in compressibility correlates with the extent of dissolution the sediment has experienced.
- Post-dissolution simple shear loading encounters lower shear stiffness and higher contractive tendency in sediments that have experienced more pronounced dissolution, in agreement with the increased state parameter. Therefore, post-dissolution sediments will be more vulnerable to excess pore pressure generation when sheared under undrained conditions.
- Regardless of the extent of dissolution (and in the absence of reprecipitation or changes in particle shape), specimens evolve towards a common ‘critical state’ strength, void ratio and fabric at large shear strains in

these simulations where the grain size distribution after dissolution (i.e. at the time of shear) is the same in all cases.

ACKNOWLEDGEMENTS

Support for this research was provided by the Department of Energy Savannah River Operations Office, the National Science Foundation and the Goizueta Foundation.

NOTATION

a_c	magnitude of anisotropy in contact orientation
a_n	magnitude of the directional variation of average normal forces
a_t	magnitude of the directional variation of tangential forces
e	void ratio
e_i	instantaneous void ratio
k_a	active earth pressure coefficient
k_0	coefficient of earth pressure at rest
M_0	initial particle mass
n	porosity
n_0	initial porosity

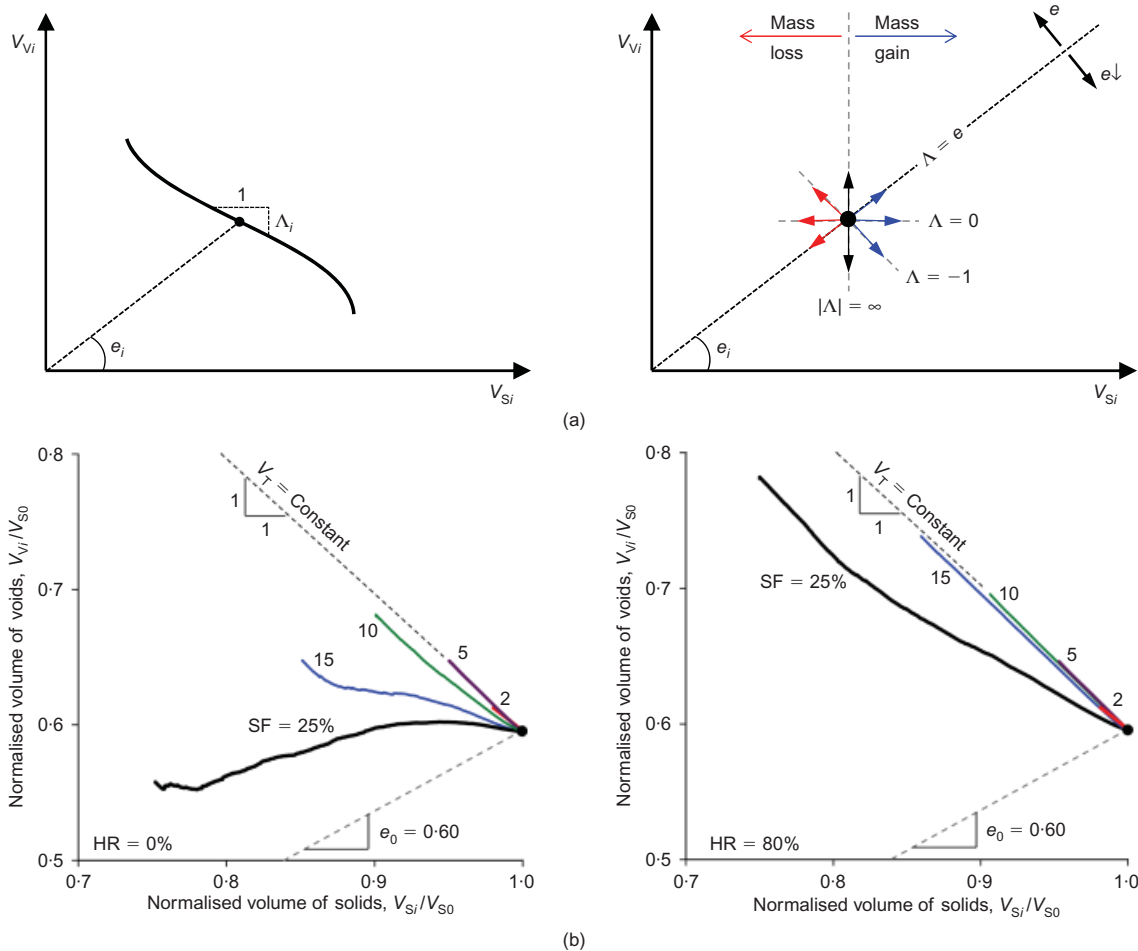


Fig. 10. Evolution in the volume of voids plotted against the volume of the solids phase during homogeneous dissolution under constant vertical stress and zero lateral stress condition: (a) interpretation guidelines; (b) data for free rotation (HR = 0% (left)) and hindered rotation (HR = 80% (right)), for different fractions of soluble particles

- R_{max} maximum particle radius
- R_{min} minimum particle radius
- R_0 initial particle radius
- S_S specific surface
- V_S volume of solid phase
- V_{Si} instantaneous volume of solid phase
- V_{S0} initial volume of solid phase
- V_T total volume
- V_{Ti} instantaneous total volume
- V_V volume of voids
- V_{Vi} instantaneous volume of voids
- ΔM_i change in instantaneous particle mass
- Δn change in porosity
- ΔR change in particle radius
- ϵ_h lateral strain
- Λ dissolution-induced void change parameter
- Λ_i instantaneous dissolution-induced void change parameter
- σ_v vertical stress

REFERENCES

Bardet, J. P. (1994). Observations on the effects of particle rotations on the failure of idealized granular materials. *Mech. Mater.* **18**, No. 2, 159–182.

Bardet, J. P. & Proubet, J. (1991). A numerical investigation of the structure of persistent shear bands in granular media. *Géotechnique* **41**, No. 4, 599–613, <http://dx.doi.org/10.1680/geot.1991.41.4.599>.

Been, K. & Jefferies, M. G. (1985). A state parameter for sands. *Géotechnique* **35**, No. 2, 99–112, <http://dx.doi.org/10.1680/geot.1985.35.2.99>.

Cartwright, J. A. & Dewhurst, D. N. (1998). Layer-bound compac-

tion faults in fine-grained sediments. *Geol. Soc. Am. Bull.* **110**, No. 10, 1242–1257.

Cha, M. (2012). *Mineral dissolution in sediments*. PhD thesis, Georgia Institute of Technology, GA, USA.

Cha, M. & Santamarina, J. C. (2013). Predissolution and postdissolution penetration resistance. *J. Geotech. Geoenviron. Engng* **139**, No. 12, 2193–2200.

Cowan, J. C. & Weintritt, D. J. (1976). *Water-formed scale deposits*. Houston, TX, USA: Gulf Publishing.

Craft, D., Cain, C. & Sullivan, C. (2006). *Seepage geochemistry and mineral dissolution at Clark Canyon dam, Pick-Sloan Missouri Basin Project, East Bench Unit, Montana*, Technical Memorandum 86–6829010. Denver, CO, USA: US Department of the Interior, Bureau of Reclamation.

Cundall, P. A. & Strack, O. D. L. (1979). Discrete numerical-model for granular assemblies. *Géotechnique* **29**, No. 1, 47–65, <http://dx.doi.org/10.1680/geot.1979.29.1.47>.

Dreybrodt, W., Romanov, D. & Gabrovsek, F. (2002). Karstification below dam sites: a model of increasing leakage from reservoirs. *Environ. Geol.* **42**, No. 5, 518–524.

Espinoza, D. N., Kim, S. H. & Santamarina, J. C. (2011). CO₂ geological storage – geotechnical implications. *KSCE J. Civ. Engng* **15**, No. 4, 707–719.

Fam, M. A., Cascante, G. & Dusseault, M. B. (2002). Large and small strain properties of sands subjected to local void increase. *J. Geotech. Geoenviron. Engng* **128**, No. 12, 1018–1025.

Ford, D. & Williams, P. W. (2007). *Karst hydrogeology and geomorphology*. Chichester, West Sussex, UK: Wiley.

Freij-Ayoub, R., Tan, C., Clennell, B., Tohidi, B. & Yang, J. H. (2007). A wellbore stability model for hydrate bearing sediments. *J. Petroleum Sci. Engng* **57**, No. 1–2, 209–220.

Gutiérrez, F., Desir, G. & Gutiérrez, M. (2003). Causes of the

- catastrophic failure of an earth dam built on gypsiferous alluvium and dispersive clays (Altorricón, Huesca Province, NE Spain). *Environ. Geol.* **43**, No. 7, 842–851.
- He, W. W., Hajash, A. & Sparks, D. (2003). Creep compaction of quartz aggregates: effects of pore-fluid flow – a combined experimental and theoretical study. *Am. J. Sci.* **303**, No. 2, 73–93.
- Herrera, M. C., Lizcano, A. & Santamarina, J. C. (2007). *Colombian volcanic ash soils, characterization and engineering properties of natural soils*, pp. 2385–2409. Singapore: Taylor & Francis.
- Iwashita, K. & Oda, M. (1998). Rolling resistance at contacts in simulation of shear band development by DEM. *J. Engng Mech. – ASCE* **124**, No. 3, 285–292.
- Iwashita, K. & Oda, M. (2000). Micro-deformation mechanism of shear banding process based on modified distinct element method. *Powder Technol.* **109**, No. 1–3, 192–205.
- Jarvis, T. (2003). *The money pit: karst failure of Anchor Dam*, Okla Geological Survey Circular 109. Norman, OK, USA: Oklahoma Geological Survey.
- Johnson, K. (2008). Gypsum-karst problems in constructing dams in the USA. *Environ. Geol.* **53**, No. 5, 945–950.
- Le Guen, Y., Renard, F., Hellmann, R., Brosse, E., Collombet, M., Tisserand, D. & Gratier, J. P. (2007). Enhanced deformation of limestone and sandstone in the presence of high P_{CO_2} fluids. *J. Geophys. Res.: Solid Earth* **112**, No. B5, 1–21.
- Lee, J. S., Tran, M. K. & Lee, C. (2012). Evolution of layered physical properties in soluble mixture: experimental and numerical approaches. *Engng Geol.* **143–144**, 37–42.
- Lee, J. Y., Santamarina, J. C. & Ruppel, C. (2010). Volume change associated with formation and dissociation of hydrate in sediment. *Geochem. Geophys. Geosystems* **11**, No. 3, Q03007.
- McDougall, J. R. & Pyrah, I. C. (2004). Phase relations for decomposable soils. *Géotechnique* **54**, No. 7, 487–493, <http://dx.doi.org/10.1680/geot.2004.54.7.487>.
- McDougall, J., Kelly, D. & Barreto, D. (2013a). Particle loss and volume change on dissolution: experimental results and analysis of particle size and amount effects. *Acta Geotechnica* **8**, No. 6, 619–627.
- McDougall, J. R., Imre, E., Barreto, D. & Kelly, D. (2013b). Volumetric consequences of particle loss by grading entropy. *Géotechnique* **63**, No. 3, 262–266, <http://dx.doi.org/10.1680/geot.SIP13.T.002>.
- Mirghasemi, A. A., Rothenburg, L. & Matyas, E. L. (2002). Influence of particle shape on engineering properties of assemblies of two-dimensional polygon-shaped particles. *Géotechnique* **52**, No. 3, 209–217, <http://dx.doi.org/10.1680/geot.2002.52.3.209>.
- Mohamed, A. & Gutierrez, M. (2010). Comprehensive study of the effects of rolling resistance on the stress–strain and strain localization behavior of granular materials. *Granular Matter* **12**, No. 5, 527–541.
- Montes-Hernandez, G., Renard, F., Geoffroy, N., Charlet, L. & Pironon, J. (2007). Calcite precipitation from CO_2 - H_2O - $Ca(OH)_2$ slurry under high pressure of CO_2 . *J. Crystal Growth* **308**, No. 1, 228–236.
- Muir Wood, D., Maeda, K. & Nukudani, E. (2010). Modelling mechanical consequences of erosion. *Géotechnique* **60**, No. 6, 447–457, <http://dx.doi.org/10.1680/geot.2010.60.6.447>.
- Payton, C. C. & Hansen, M. N. (2003). *Gypsum karst in south-western Utah: failure and reconstruction of Quail Creek Dike*, Okla Geological Survey Circular 109. Norman, OK, USA: Oklahoma Geological Survey.
- Pearson, R. M. (2002). Gypsum karst of the Lykins Formation and effects for Colorado Front Range water projects; Horsetooth and Carter Lake Reservoirs. *Geol. Soc. Am. Abstr. Programs* **34**, No. 6, 216.
- Renard, F., Gundersen, E., Hellmann, R., Collombet, M. & Le Guen, Y. (2005). Numerical modeling of the effect of carbon dioxide sequestration on the rate of pressure solution creep in limestone: preliminary results. *Oil Gas Sci. Technol. – Rev. Inst. Français Petrole* **60**, No. 2, 381–399.
- Rothenburg, L. & Bathurst, R. J. (1989). Analytical study of induced anisotropy in idealized granular-materials. *Géotechnique* **39**, No. 4, 601–614, <http://dx.doi.org/10.1680/geot.1989.39.4.601>.
- Rothenburg, L. & Bathurst, R. J. (1993). Influence of particle eccentricity on micromechanical behavior of granular-materials. *Mech. Mater.* **16**, No. 1–2, 141–152.
- Rothwell, R. G., Thomson, J. & Kahler, G. (1998). Low-sea-level emplacement of a very large Late Pleistocene ‘megaturbidite’ in the western Mediterranean Sea. *Nature* **392**, No. 6674, 377–380.
- Shin, H. & Santamarina, J. C. (2009). Mineral dissolution and the evolution of k_0 . *J. Geotech. Geoenviron. Engng* **135**, No. 8, 1141–1147.
- Shin, H., Santamarina, J. C. & Cartwright, J. A. (2008). Contraction-driven shear failure in compacting uncemented sediments. *Geology* **36**, No. 12, 931–934.
- Stefanou, I. & Sulem, J. (2014). Chemically induced compaction bands: triggering conditions and band thickness. *J. Geophys. Res.: Solid Earth* **119**, No. 2, 880–889.
- Suiker, A. S. J. & Fleck, N. A. (2004). Frictional collapse of granular assemblies. *J. Appl. Mech.* **71**, No. 3, 350–358.
- Sultan, N., Cochonat, P., Canals, M., Cattaneo, A., Dennielou, B., Hafidason, H., Laberg, J. S., Long, D., Mienert, J., Trincardi, F., Urgeles, R., Vorren, T. O. & Wilson, C. (2004). Triggering mechanisms of slope instability processes and sediment failures on continental margins: a geotechnical approach. *Mar. Geol.* **213**, No. 1–4, 291–321.
- Thomas, P. A. & Bray, J. D. (1999). Capturing nonspherical shape of granular media with disk clusters. *J. Geotech. Geoenviron. Engng* **125**, No. 3, 169–178.
- Tran, M. K., Shin, H., Byun, Y.-H. & Lee, J.-S. (2012). Mineral dissolution effects on mechanical strength. *Engng Geol.* **125**, 26–34.
- Truong, Q. H., Eom, Y. H. & Lee, J. S. (2010). Stiffness characteristics of soluble mixtures. *Géotechnique* **60**, No. 4, 293–297, <http://dx.doi.org/10.1680/geot.8.T.032>.
- Unay, G., Ertunc, A., Bulutlar, E. & Akdogan, E. (1982). Karstic limestone problem at Kavsak dam site and reservoir area. *Bull. Engng Geol. Environ.* **25**, No. 1, 143–150.
- Vogt, P. R. & Jung, W. Y. (2002). Holocene mass wasting on upper non-polar continental slopes – due to post-glacial ocean warming and hydrate dissociation. *Geophys. Res. Lett.* **29**, No. 15, 1–4.
- Waltham, T. (2009). *Foundations of engineering geology*. New York, NY, USA: Spon.
- Watson, M. N., Boreham, C. J. & Tingate, P. R. (2004). Carbon dioxide and carbonate cements in the Otway Basin: Implications for geological storage of carbon dioxide. *APPEA J.* **44**, 703–720.
- Zheng, B. & Elsworth, D. (2012). Evolution of permeability in heterogeneous granular aggregates during chemical compaction: granular mechanics models. *J. Geophys. Res.: Solid Earth* **117**, No. B3, B03206.